Single-Exposure Contrast-Enhanced Spectral Mammography

Raul Torrico[a], Amar Kavuri[b], Cale Lewis[a] and Mini Das[a,b]

[a]Department of Physics, University of Houston, Houston, Texas 77204
[b]Department of Biomedical Engineering, University of Houston, Houston, Texas 77204

ABSTRACT

Contrast-enhanced spectral mammography (CESM) is being implemented to overcome the limitations of conventional mammography where tumor visualization is obstructed by overlapping glandular tissue. CESM exploits the spectral properties of a contrast agent by subtracting two images one obtained above and other below the K-edge energy. The most common approach requires dual-exposure where two images are obtained with different incident spectra. However, this comes at the expense of increased patient dose and susceptibility to motion artifacts. We propose the use of photon counting spectral detectors to simultaneously obtain multiple images with single-exposure. This is demonstrated using a wide area CdTe Medipix3RX detector to acquire images of iodine contrast agent in an anthropomorphic breast imaging phantom. The electronic thresholds in the detector replace the traditional physical filters. Our results show single-exposure CESM for the detection of iodine with concentrations as low as 2.5 mg/mL of a 10 mm diameter target in a 5 cm thick heterogeneous background. These results demonstrate the viability of photon counting detectors for low dose contrast-enhanced mammography.

Keywords: Contrast-Enhanced mammography, Spectral mammography, Photon counting detectors

1. INTRODUCTION

Digital mammography (DM) has become the number one tool for effective cancer screening. The sensitivity and specificity of DM is heavily dependent on the density of the breast.[1,2] One of the primary challenges in DM is to enhance the visibility of unhealthy tissue, tumor and microcalcifications, which can be hidden by the overlap of adjacent healthy, glandular and adipose, in the breast[1].[3] Also, the small difference in x-ray linear attenuation coefficient between tumor and breast tissue has led to novel methods to enhance the tumor.

Dual energy subtraction methods are performed to enhance the visualization of low contrast objects through the removal of the background. The method exploits the K-edge of a contrast agent, such as iodine, to produce a contrast-enhanced image in mammography.[4–7] In conventional dual energy imaging, the high and low energy images are acquired above and below the contrast agent's K-edge. This is done to maximize the difference in signal from the contrast agent, and minimize the difference in signal from the breast background. Typically, the process involves high and low kVp exposures and the use of physical filters to reduce spectral overlap. However this increases the dose to the patient. An example of two kVp exposures that potentially could be used for dual energy imaging is shown in Fig. 1.

Clinical examinations uses energy integrating detectors that are unable to differentiate higher energy photons from lower energy photons, resulting in sub-optimal results.[8] An experimental set-up proposed for single-shot acquisition is to utilize flat panel dual-layer detectors,[9] and to reduce the dose. The front layer absorbs primarily low-energy x-ray photons while the rear layer absorbs primarily high-energy photons. Depending on the type of the dual-layer detector, complete spectral separation might be insufficient,[10,11] as some high energy photons would be detected by the front layer and vice versa.

Energy resolving detectors are being considered for the contrast-enhanced mammography as they can measure the two images above and below the K-edge simultaneously.[?] These detectors have been also been investigating other applications such as phase contrast,[12] material decomposition[13] and CT. We propose and demonstrate the use of electronic energy thresholds in a photon counting spectral detectors (PCD) in lieu of physical filters, thereby potentially allowing a single exposure contrast-enhanced mammography. Our results are demonstrated using a photon counting detector with CdTe sensor. This phantom study utilized three different iodinated concentrations with a CIRS Model 020 BR3D Breast Imaging Phantom.

For further information, Email: mdas@uh.edu

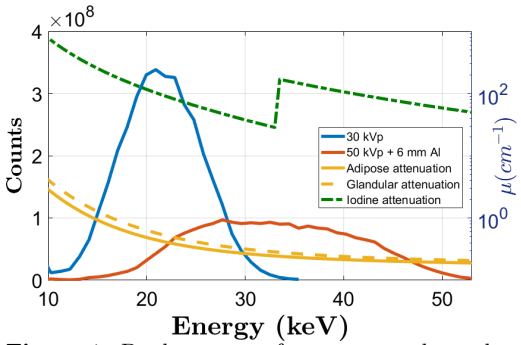

Figure 1: Dual spectrum for contrast-enhanced mamography. Figure also shows the NIST linear attenuation of iodine, adipose and glandular tissue.

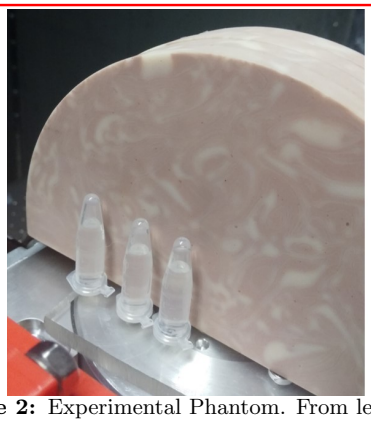

Figure 2: Experimental Phantom. From left to right: 10, 5, 2.5 mg/mL Iodine with CIRS breast phantom as background.

2. MATERIALS AND METHODS

2.1 Materials

The images were acquired using a micro-focus x-ray tube (L8121-03) from Hamamatsu with a Tungsten anode. A 50 kVp beam with an additional 0.25 mm Al filter was used as it is within the clinical mammography and general radiographic x-ray energy ranges.[14] The tube loading used was 15 mAs. The contrast agent for this study was iodine as its K-edge falls within the energy range used for clinical mammography. Three concentrations of iodine were used: 10, 5 and 2.5 mg/mL. Each concentration was housed inside of a cylindrical container of radius of 10.53 mm. An anthropomorphic breast phantom from CIRS was used as background with a total thickness of 5 cm, which is the average breast size.[15] Each slab contains two tissue equivalent materials mimicking 100 % adipose and 100% gland tissues together in an approximate 50/50 ratio by weight. Fig. 2 shows a picture of the phantom. The source-to-sample and sample-to-detector distances were 40cm and 5cm respectively.

2.2 Image Acquisition

A wide area photon counting detector was used for the experiments. The Widepix detector (ADVACAM s.r.o, Prague, CZ) is composed of an array of five CdTe Medipix3RX units, with an effective size of 256x1,280 pixels with a 55 μm pitch. The sensor is 1000 μm thick. It is operated in charge summing mode (CSM) for charge sharing correction. When operated in spectroscopic mode, the effective pixel pitch is 110 μm. In spectroscopic mode, up to 4 energy thresholds can be simultaneously utilized by the detector to gain spectral information. These thresholds correspond to incident photon energies and dictate the minimum energies necessary for photons to trigger counts in the detector. Our recently proposed robust energy calibration technique was used to determine these threshold energies.[16]

Photon counting detectors use electronic energy thresholds to discriminate photons based on their energies. For a given threshold, incident photons whose energies lie below the threshold energy are not registered as counts in the detector. By setting a threshold, the user can collect all the photons with energy higher than the corresponding threshold. By scanning the threshold in this way, one obtains an integral spectrum (Fig. 3a). This integral mode data can be differentiated to obtain true counts corresponding to each threshold or to that of smaller energy bins, producing an X-ray spectrum (Fig. 3b).

Detailed spectroscopic mode acquisition and effective attenuation are given in Eqn. 4, 5 and 6. The unattenuated intensity I_0^{int}, or the flat-field, for the integral energy threshold E_i is described by

$$I_0^{int}(E_i) = \int_{E_i}^{kVp} \Phi(E)D(E)dE, \tag{1}$$

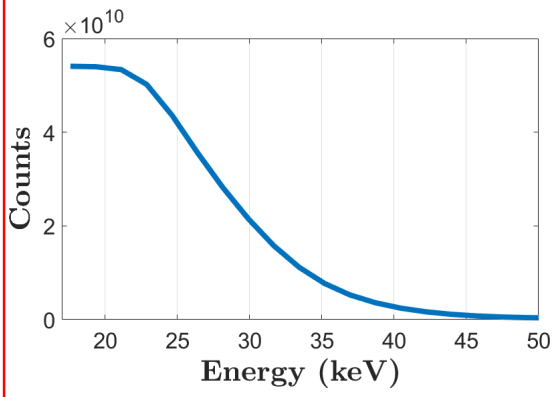

(a) Measured integral spectrum obtained of the X-ray tungsten source anode using the Widepix detector.

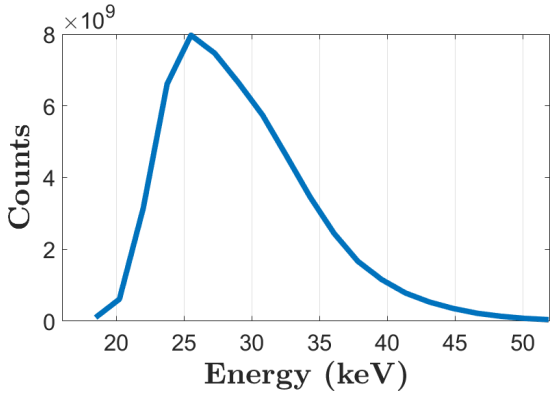

(b) Differential spectrum of the X-ray tungsten source anode using the Widepix detector.

Figure 3

where $\Phi(E)$ is the photon flux, D(E) is detector response function. In our application, E_i will correspond to either the low or high threshold energies.

And the attenuated intensity from some object, I^{int}, is given by

$$I^{int}(E_i) = \int_{E_i}^{kVp} e^{-\int \mu(E)dT} \Phi(E)D(E)dE, \tag{2}$$

where $\mu(E)$ and T are the linear attenuation coefficient and thickness of the target.

Similarly, the unattenuated intensity I_0^{spec} for the spectral or binned energy threshold E_b is described by

$$I_0^{spec}(E_b) = I_0^{int}(E_i) - I_0^{int}(E_{i+1}) \tag{3}$$

$$= \int_{E_i}^{E_{i+1}} \Phi(E)D(E)dE \tag{4}$$

and the resulting attenuated intensity for the spectral data follows the same description

$$I^{spec}(E_b) = \int_{E_i}^{E_{i+1}} e^{-\int \mu(E)dT} \Phi(E)D(E)dE, \tag{5}$$

The effective linear attenuation was calculated by using the equation:

$$\bar{\mu}_{spec}(E_b) = -\frac{1}{T}\, ln\, \frac{I^{spec}(E_b)}{I_0^{spec}(E_b)} \tag{6}$$

For our particular experiment, the resulting iodine-only subtracted image, S_{DE} is obtained by using the weighted logarithmic subtraction method.

$$S_{DE}^{spec} = -ln\, I_h^{spec} + R\, ln\, I_l^{spec} \tag{7}$$

In which I_l and I_h represent the flat-field corrected low and high energy binned images respectively. In this paper, the weighting factor R is experimentally determined to remove the breast imaging phantom background. The optimal weighting factor R is defined[17] as:

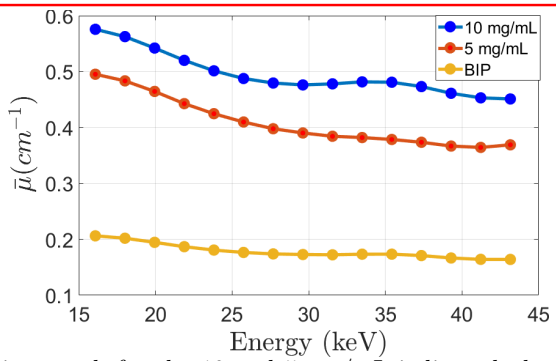

Figure 4: Effective attenuation graph for the 10 and 5 mg/mL iodinated phantoms and the breast imaging phantom (BIP).

$$R = \frac{\bar{\mu}_{b,h}}{\bar{\mu}_{b,l}} \tag{8}$$

In which $\bar{\mu_b}$ is the estimated attenuation of the average breast background of the high and low bin images. However, full cancellation may not be achievable due to the multiple tissue types present in the background of adipose and glandular tissue with slightly varying attenuation properties.

The figure of merit chosen to evaluate the dual energy subtracted images was the signal to noise ratio (SNR). The equation is given as:

$$SNR = \frac{|S^{spec}_{DE,c} - S^{spec}_{DE,b}|}{\sqrt{\sigma^2_{DE,c} + \sigma^2_{DE,b}}} \tag{9}$$

where σ represents the noise for both the iodine contrast and breast imaging phantom background. S_{DE} is the mean signal from the iodine contrast and the breast imaging phantom as defined in eqn 7. The iodine signal for the 10 mg/mL vial and noise were measured using a R.O.I. of 101 x 19 pixels, where the thickness is relatively constant. The R.O.I. for breast imaging phantom signal and the noise had a size of 101 x 39 pixels.

3. RESULTS

In order to maximize the K-edge contrast, ideally two monochromatic sources would be required. However in practice, we work with polychromatic sources in clinics. The experimentally measured K-edge for 10 and 5 mg/mL iodine is shown in Fig. 4. Instead of having a sharp discontinuity, the K-edge response spans several keVs due to the detector's limited energy resolution. Similarly, for decreasing concentrations of iodine, the K-edge signal is diminished. Thus making K-edge subtraction a challenge to locate the K-edge and properly place the high and low energy bins for the subtraction.

The importance of selecting the appropriate energy bin combinations would affect the final contrast-enhanced subtracted image. Assuming a perfect cancellation of the background, as seen on Fig. 4, since the measured linear attenuation of the breast imaging phantom is relatively constant in the spectral range of 15-45 keV. The SNR would be only dependent on signal difference $S_{DE,c}$ from the average iodine linear attenuations from the high and low energy bin (Eq. 9). Based on our experiments, it was determined the optimal placement for the high energy bin should be above the K-edge, around that of 35 keV.

Similarly, the placement and size of the low energy bin would affect the measured SNR. It has been shown that images obtained by utilizing a narrow energy window will feature maximum contrast but large noise. Images obtained with a wide energy bin will feature high statistics, and hence low noise, but poorer contrast.[18] In general, depending on the placement and/or bin width of the low energy image, with the high energy bin image's position close to the K-edge, a local maximum SNR can be found for that particular combination.

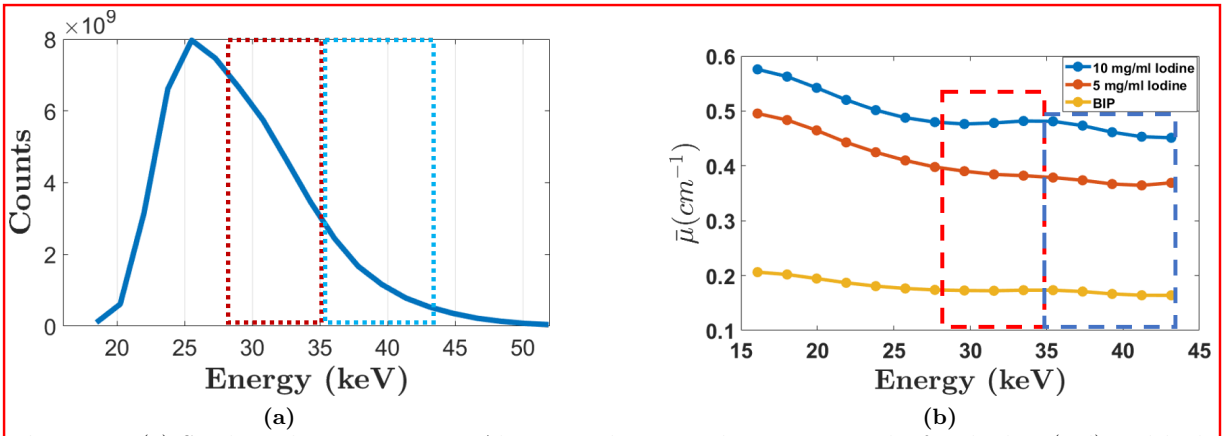

(a) (b)

Figure 5: (a) Single 50 kVp + 0.25 mm Al spectra depicting the spectrum split for the low (red) and high energy (blue) images. (b) Effective attenuation graph highlighting optimal low and high energy combinations.

For our experiment, Fig. 5a represents graphically the split of the spectrum with the bin position and bin size of the high and low energy bins. The low energy bin is the size of 28-35 keV, with a width of 7 keV, with its mean energy of 31.7 keV. The high energy bin size is from 35-44 keV, with a width of 9 keV with a mean energy of 36.6 keV. Similarly, Fig 5b shows the mean attenuation graph with the corresponding optimal high and low energy bins.

Only one acquisition of the low and high energy images was performed by setting the appropriate thresholds from SNR measurements for the 10 mg/mL iodine contrast. Both low and high energy images were acquired with a 30 second collection time each. Fig. 6a is the logarithmic flat-field corrected low energy image with a median filter of kernel size of 5x5 was applied. The glandularity striations can be observed across the iodine vials. We observe that the three varying concentrations of iodine show the same attenuation intensities due to the distribution of glandular/adipose on the breast slabs in certain regions (Fig. 6b). Thus, the weighted logarithmic subtraction (Eqn. 7) is applied. The optimal weighting factor R was experimentally measured for each breast region. An average weighting factor R of was determined to be 0.82 using the method described in Eq. 8 to cancel out the breast tissue.

It is known the resulting subtracted image would have higher noise compared to the high and low energy images.[8] To mitigate the noise, a similar median filter was applied to the high energy image. The weighted logarithmic subtracted image is shown in Fig. 7a after additional Wiener filter was applied. The SNR measured was found to be 4.3, 2.88, 1.68 for the for the 10, 5, and 2.5 mg/mL iodine respectively.

The optimal weighting factor R effectively removed the overlapping glandularity from the image. Only regions containing the iodine contrast are shown, thus indicating only areas without iodine uptake were removed. Observing Fig. 7b, we see the average breast background is zero. We are now able to qualitatively differentiate the different concentrations of iodine. In particular, for the 2.5 mg/mL Iodine concentration in which a weak K-edge signal is expected.

4. CONCLUSION

In conclusion, we demonstrated the first preliminary results showing feasibility of a single-shot contrast enhanced mammography. A Widepix CdTe photon counting detector in spectroscopic mode acquisition was used to obtain these results. In addition, the electronic thresholds in the spectral detector served as bin separating filters in this study. For our experiment, down to 2.5 mg/mL of iodine was identified in our study with an anthropomorphic breast phantom. This concentration is below the minimum iodine concentrations of 3 to 4 mg/mL which have been found reasonable for tumor uptake, assuming a 10 mm thick tumor.

These preliminary results points to the feasibility of low dose contrast-enhanced mammography with a Widepix CdTe detector. The results will be compared against conventional dual energy imaging via simulations and

Figure 6

(a) Logarithmic flat-field corrected low energy image. Visible are the glandular striations. 1) 2.5 mg/mL, 2) 5 mg/mL, 3) 10 mg/mL Iodine.

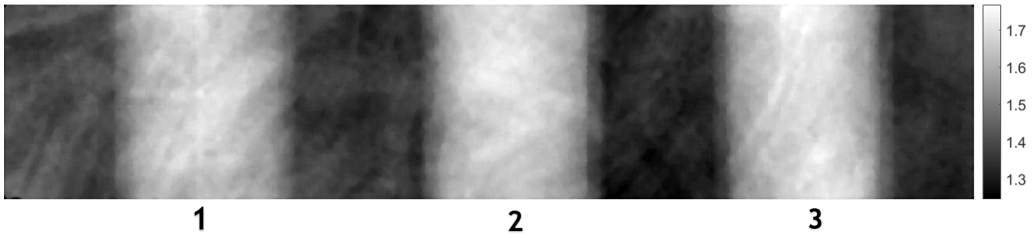

(b) Average projected attenuation line profile of the low energy image.

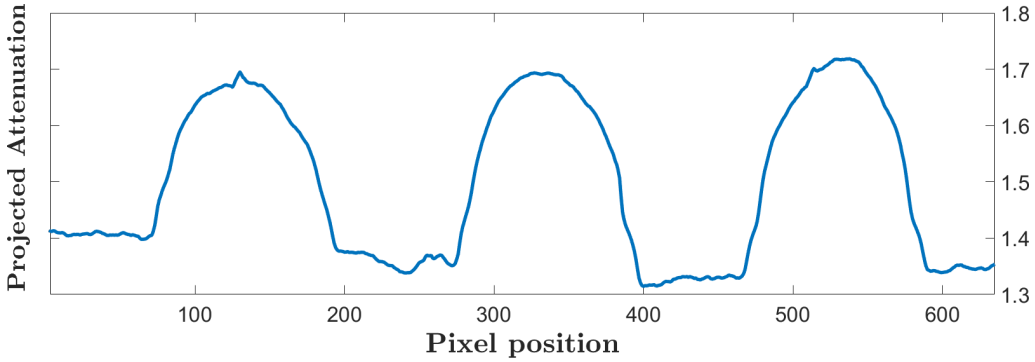

Figure 7

(a) Weighted logarithmic subtracted image.

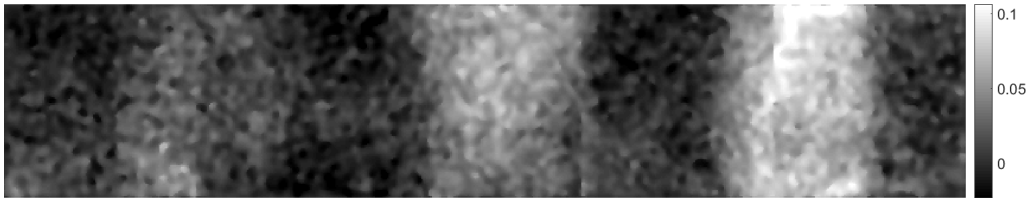

(b) Average projected attenuation difference line profile.

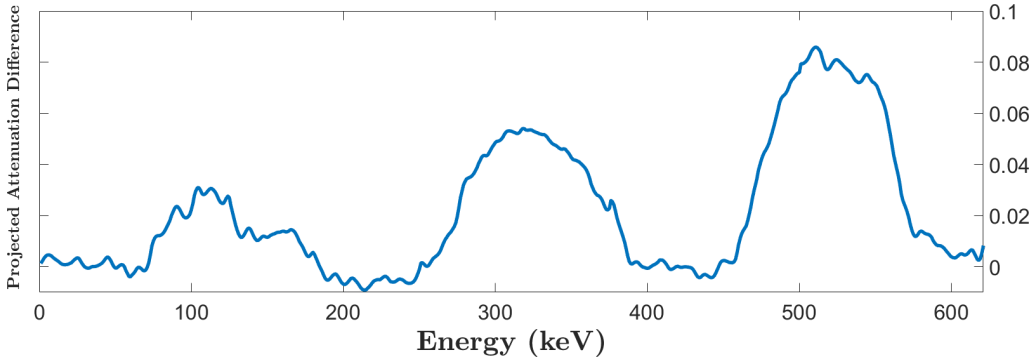

phantom studies for dose and image quality. In addition, we will be comparing our results using a clinical mammography tube and the WidePix detector.

5. ACKNOWLEDGMENTS

We would like to thank Medipix collaborations and several members for their valuable discussions. This work was partially supported by funding from the US Department of Defense (DOD) Congressionally Directed medical Research Program (CDMRP) Breakthrough Award BC151607 and the National Science Foundation CAREER Award 1652892.

REFERENCES

1. E. D. Pisano, C. Gatsonis, E. Hendrick, M. Yaffe, J. K. Baum, S. Acharyya, E. F. Conant, L. L. Fajardo, L. Bassett, C. D'Orsi, R. Jong, and M. Rebner, "Diagnostic Performance of Digital versus Film Mammography for Breast-Cancer Screening," *New England Journal of Medicine* **353**, pp. 1773–1783, oct 2005.
2. E. Luczyńska, S. Heinze, A. Adamczyk, J. Rys, J. Mitus, and E. Hendrick, "Comparison of the Mammography, Contrast-Enhanced Spectral Mammography and Ultrasonography in a group of 116 patients," *Anticancer Research* **36**, pp. 4359–4366, 2016.
3. T. Asaga, C. Masuzawa, A. Yoshida, and H. Matsuura, "Dual-energy subtraction mammography," *Journal of Digital Imaging* **8**(1 Supplement), pp. 70–73, 1995.
4. H. Bornerfalk and M. Hemmendorff, "Contrast-enhanced dual-energy mammography using a scanned multislit system: evaluation of a differential beam filtering technique," *Journal of Electronic Imaging* **16**(2), p. 023006, 2007.
5. A. K. Carton, C. Ullberg, K. Lindman, T. Francke, and A. Maidment, "Optimization of a dual-energy contrast-enhanced technique for a photon counting digital breast tomosynthesis system," *Lecture Notes in Computer Science (including subseries Lecture Notes in Artificial Intelligence and Lecture Notes in Bioinformatics)* **5116 LNCS**, pp. 116–123, 2008.
6. M. Zankl, D. R. Dance, C. L. Skinner, R. Klein, H. Aichinger, F. I. N. Breast, and T. U. Mcnpx, "Physics in Medicine & Biology Backscatter factors for mammography calculated with Monte Carlo methods Backscatter factors for mammography calculated with Monte Carlo methods," *Phys. Med. Bio* **46**(10), pp. 771–781, 2001.
7. M. Lundqvist, B. Cederström, V. Chmill, M. Danielsson, and B. Hasegawa, "Evaluation of a photon-counting X-ray imaging system," *IEEE Transactions on Nuclear Science* **48**(4 II), pp. 1530–1536, 2001.
8. S. Faby, S. Kuchenbecker, S. Sawall, D. Simons, H.-P. Schlemmer, M. Lell, and M. Kachelrieß, "Performance of today's dual energy CT and future multi energy CT in virtual non-contrast imaging and in iodine quantification: A simulation study," *Medical Physics* **42**(7), pp. 4349–4366, 2015.
9. J. C. Han, H. K. Kim, D. W. Kim, S. Yun, H. Youn, S. Kam, J. Tanguay, and I. A. Cunningham, "Single-shot dual-energy x-ray imaging with a flat-panel sandwich detector for preclinical imaging," *Current Applied Physics* **14**(12), pp. 1734–1742, 2014.
10. E. Fredenberg, "Spectral and dual-energy X-ray imaging for medical applications," *Nuclear Instruments and Methods in Physics Research, Section A: Accelerators, Spectrometers, Detectors and Associated Equipment* **878**(August 2017), pp. 74–87, 2018.
11. T. P. Szczykutowicz and W. Madison, "Dual-Energy and Spectral Imaging," *Comprehensive Biomedical Physics* , pp. 155–166, 2014.
12. D. Gürsoy and M. Das, "Single-step absorption and phase retrieval with polychromatic x rays using a spectral detector," *Optics Letters* **38**(9), p. 1461, 2013.
13. N. R. Fredette, C. E. Lewis, and M. Das, "A multi-step method for material decomposition in spectral computed tomography," *Proceedings of SPIE Medical Imaging* **10132**, p. 101321C, 2017.
14. W. R. Brody, "Digital subtraction angiography," *IEEE Transactions on Nuclear Science* **29**(3), pp. 1176–1180, 1982.
15. Sabee Molloi, H. Ding, and S. Molloi, "Quantification of breast density with spectral mammography based on a scanned multi-slit photon-counting detector: A feasibility study," *Physics in Medicine and Biology* **57**(15), pp. 4719–4738, 2012.

16. S. Vespucci, C. Park, R. Torrico, and M. Das, "Robust Energy Calibration Technique for Photon Counting Spectral Detectors," *IEEE Transactions on Medical Imaging* , 2018.
17. I. Rosado-Mendez, B. A. Palma, and M. E. Brandan, "Analytical optimization of digital subtraction mammography with contrast medium using a commercial unit," *Med. Phys* **35**(12), 2008.
18. S. Pani, S. C. Saifuddin, C. Christodoulou, M. C. Veale, P. Seller, R. D. Speller, M. D. Wilson, and J. W. Scuffham, "K-edge subtraction imaging using a pixellated energy-resolving detector," *Physics* **7961**, pp. 79614C–79614C–8, 2011.